Separation and Purification Technology 334 (2024) 125987

Contents lists available at ScienceDirect

Separation and Purification Technology

journal homepage: www.elsevier.com/locate/seppur

A stable ultramicroporous Cd(II)-MOF with accessible oxygen sites for efficient separation of light hydrocarbons with high methane production

Xing-Zhe Guo [a,b,1], Bingwen Li [a,1,*], Guang-Zu Xiong [b,1], Bing Lin [c], Liu-Cheng Gui [c], Xiao-Xia Zhang [b], Zhihui Qiu [c], Rajamani Krishna [d], Xinfang Wang [a], Xin Yan [a,*], Shui-Sheng Chen [b,*]

[a] Shandong Key Laboratory of Biophysics, Institute of Biophysics, College of Chemistry and Chemical Engineering, College of Medicine and Nursing, Dezhou University, Dezhou 253023, PR China
[b] Engineering Research Center of Oligosaccharides, Fuyang Normal University, Fuyang 236041, China
[c] School of Chemistry & Pharmaceutical Sciences, Guangxi Normal University, Guilin, Guangxi 541004, China
[d] Van't Hoff Institute for Molecular Sciences, University of Amsterdam, the Netherlands

ARTICLE INFO

Keywords:
Metal-organic frameworks
Separation of light hydrocarbons
Dynamic breakthrough experiment
GCMC simulations

ABSTRACT

Metal-organic frameworks (MOFs) have garnered increasing attention for their effective separation of light hydrocarbons owing to their prominent separation selectivity and energy-efficient adsorption process. Here, we constructed a robust stable ultramicroporous Cd(II)-MOF ($[Cd_5(NTA)_4(H_2O)_2]$ $(Me_2NH_2^+)_2{\cdot}10H_2O$ (**1**)) with abundant accessible oxygen sites and investigated its adsorption performance for recovering high-purity methane (CH_4) from natural gas (NG) including $C_1(CH_4)/C_2(C_2H_6)/C_3(C_3H_8)$ mixtures. At ambient conditions, the theoretical equilibrium separation selectivity of **1** for C_2H_6/CH_4 (v/v = 10/85) and C_3H_8/CH_4 (v/v = 5/85) were found to be 34.3 and 223.8, respectively. The $CH_4/C_2H_6/C_3H_8$ (v/v/v = 85/10/5) mixture breakthrough experiments for **1**, conducted at 298 K, demonstrated effective separation performance with breakthrough times of up to 136 and 280 $min{\cdot}g^{-1}$ for C_2H_6 and C_3H_8. Particularly, the CH_4 productivity (purity > 99.9 %) with 9.8 $mmol{\cdot}g^{-1}$ ranked the third in reported literatures, lower to the reported maximum value of 13.28 $mmol{\cdot}g^{-1}$ for $Ni(TMBDC)(DABCO)_{0.5}$. Furthermore, Grand Canonical Monte Carlo (GCMC) simulations and first-principles density functional theory (DFT) calculations revealed that the high uptake and selectivity for C_3H_8 and C_2H_6 can be attributed to the abundant oxygen sites present in the pores. The dynamic breakthrough experiments comprehensively demonstrated that the proposed MOF can be an effective potential adsorbent for the practical separation of $CH_4/C_2H_6/C_3H_8$ mixtures.

1. Introduction

Natural gas (NG), a crucial source of clean energy, is an important chemical raw material, primarily comprising methane (CH_4) along with variable amounts (~20 %) of ethane (C_2H_6) and propane (C_3H_8). CH_4 is a popular fuel source, when high-purity CH_4 undergoes oxidized coupling transformation, it produces the highly valuable electronic gas ethyne (C_2H_2). Additionally, C_2H_6 and C_3H_8 serve as vital feedstocks for the production of olefins used in the synthesis of polyethylene materials [1–3]. Thus, the complete utilization of these hydrocarbons through CH_4 purification and C_3H_8/C_2H_6 recovery from single/double/triple carbon ($C_1/C_2/C_3$) light hydrocarbon mixtures can have enormous commercial value. However, as light hydrocarbon compounds exhibit almost identical sizes and similar physical properties, their effective separation and purification can be quite difficult to achieve. Traditional cryogenic distillation with energy-intensive separation is suitable for separating the different components of light hydrocarbon mixtures, but it requires high operational requirements, low automation, strict safety measures, and large monetary investments. Particularly, the high energy consumption of these methods leads to a serious departure from the two-carbon policy [4,5].

Recently, metal–organic frameworks (MOFs) have emerged as porous materials to employ in gas separation and purification due to their superior performance for the capture of hydrocarbons with high

* Corresponding authors.
E-mail addresses: libingwen0609@163.com (B. Li), yanxin2012@iccas.ac.cn (X. Yan), chenss@fynu.edu.cn (S.-S. Chen).
[1] Equal contribution.

https://doi.org/10.1016/j.seppur.2023.125987
Received 5 August 2023; Received in revised form 26 November 2023; Accepted 6 December 2023
Available online 10 December 2023

capacity and selectivity [6–10]. Therefore, extensive research has led to the development of targeted MOFs functionalized with open metal or organic functional active sites to separate light hydrocarbon mixtures in a cost-effective and environmentally sustainable manner [11–15]. Recently, much progress has been made to separate C_1-C_3 light hydrocarbon mixtures. The most representative MOF Fe_2(dobdc) has an adsorption selectivity in the range of 13–18 for C_2H_6/C_2H_4 mixtures, obtaining 99–99.5 % purity for C_2H_4 at 318 K, because the adsorption site of Fe-C distances between open metal Fe sites and guest C_2H_4 fall in the range of 2.39–2.59 Å [16]. Borah's group explored the $C_1/C_2/C_3$ mixtures separation performance of the landmark MOF Cu-BTC as well as the equimolar binary mixtures of CH_4/C_2H_6 and CH_4/C_3H_8 [17]. Also, the Cu-BTC ever holding the record of the highest CH_4 adsorption had good separation performance for $C_1/C_2/C_3$ ternary mixtures. The novel-designed MOF ECUT-Th-10 with unique six-fold imide-sealed pockets is beneficial to separate C_3H_8 from the $CH_4/C_2H_6/C_3H_8/C_4H_{10}$ mixture because the pocket-like cage not only presents molecular sieving effect compared with more bulk C_4H_{10}, while imide units decorated in the pocket-like cages afford multiple (C)H(δ^+)···(δ^-)O(C) interactions with C_3H_8, hence enforcing the interactions between guest and host-framework for C_3H_8 [18]. The porous Cu-IPA shows good $CH_4/C_2H_6/C_3H_8$ separation performance and adsorption selectivity and different retention times from breakthrough experiments, which can be elucidated to abundantly accessible oxygens of C—H···O interactions in the triangular channel for different polarizability of C_2H_6 and C_3H_8 by the molecular simulation [19]. The MOF Ni(TMBDC)(DABCO)$_{0.5}$ designed by Li group possessed remarkably high adsorption uptakes of 3.37 and 2.93 mmol·g^{-1} for C_3H_8 and C_2H_6, as well as a high adsorption selectivity up to 274 and 29 for C_3H_8/CH_4 and C_2H_6/CH_4, respectively. Molecular simulations reveal that these characteristics can be ascribed to the strong interaction between the functionalized methylene (CH_2) and methyl (CH_3) groups and the guest C_3H_8 and C_2H_6 molecules within Ni(TMBDC)(DABCO)$_{0.5}$ channels [20]. Interestingly, we have elaborately designed a stable microporous Ni(II)-MOF based on the ligand functionalized by the hydroxy group, possessing multiple accessible adsorption sites benefiting both high gas uptake and effective separation for light hydrocarbons, and the adsorption selectivity for C_3H_8/CH_4, C_3H_8/C_2H_6, and C_2H_6/CH_4 lie in the range of 638.9–370.5, 10.9–3.5, and 61.0–35.1. Moreover, the breakthrough experiments for equimolar ternary $CH_4/C_2H_6/C_3H_8$ mixture showed breakthrough times of 2.6, 35, and 190 min, respectively, achieving effective separation of the $C_1/C_2/C_3$ components. Significantly, GCMC simulation confirms the synergistic host–guest interactions from functional OH groups, carboxylate groups, and $HCOO^-$ groups [21]. As an extension of our previous work, this work aims to construct an ultramicroporous Cd(II)-MOF with accessible oxygen sites to investigate the potential as gas adsorbents for CH_4 separation in C_1-C_3 mixed feedstocks. The porous Cd(II)-MOF was constructed based on the 4,4′,4″-tricarboxytriphenylamine (H_3NTA) ligand with C_3 symmetry. Interestingly, the pentanuclear Cd_5(II) clusters were bridged with carboxylate groups to form ultramicroporous with bridged carboxyl groups acting as oxygen active sites. The adsorption selectivity for C_2H_6/CH_4 and C_3H_8/CH_4 at 298 K was 34.3 and 223.8, and particularly, the CH_4 adsorption capacity reaches 9.8 mmol·g^{-1}, lower than the highest value of 13.28 mmol·g^{-1} for Ni (TMBDC)(DABCO)$_{0.5}$ [20], ranking the third as the reported values in the literatures. Dynamic breakthrough experiments comprehensively demonstrated the promising potential of **1** as an adsorbent for practical $CH_4/C_2H_6/C_3H_8$ separation. Furthermore, GCMC simulations and DFT calculations revealed that the high capture and selectivity of **1** for C_3H_8 and C_2H_6 can be attributed to the abundant oxygen sites in the channels.

2. Experimental

2.1. General information and materials

The detailed description for the experimental materials and instruments is listed in the Supplementary Material.

2.2. Synthesis of [$Cd_5(NTA)_4$ $(H_2O)_2$]($Me_2NH_2^+$)$_2$·10H_2O (1)

The synthesis of MOF **1** is referred to the literature with slight change [18]. H_3NTA (15.0 mg) and $Cd(NO_3)_2·4H_2O$ (20.0 mg) were added into a 20 mL Teflon-lined steel vessel, following 1.5 mL dimethyl formamide, 1.5 mL ethanol and 0.5 mL HBF_4 were added to dissolve the ligand, and heated at 80 °C for 48 h. Yellow bulk crystals were obtained with a yield of 62 %. Anal. (%) calcd. for $C_{88}H_{88}Cd_5N_6O_{36}$: C, 85.99; H, 7.17; N, 6.84. Found: C, 86.05; H,7.12; N, 6.83. IR (KBr pellet, cm $^{-1}$): 3444(vs), 1590 (vs), 1399(vs), 1313 (s), 1271(m), 1171(m), 851(m), 782(m), 681(m), 521(m).

2.3. Gas adsorption measurements

The solvent-exchanged sample was obtained from the as-synthesized sample **1** by soaked in fresh ethanol for 1 day and exchanged for three times. The treated sample was activated for 12 h at evacuated (<10^{-3} torr). The gas adsorption isotherms were carried out on a Quantachrome Autosorb-iQ. Ultrahigh-purity-grade (>99.999 %) N_2, CH_4, C_2H_6 and C_3H_8 gases were used in all measurements.

3. Results and discussion

3.1. Structural description of 1

Crystallographic analysis showed that **1** crystallized in monoclinic system, with the space group of *P2$_1$/c*. The structure is similar to the literature reported by Zhu's group [22]. The asymmetric unit contains two and a half of crystallographically independent Cd(II) atoms, two NTA^{3-} ligands, and a protonated $Me_2NH_2^+$, in this sense, the total charges of the framework are balanced. It is worth mentioning that in the structure, the Cd1, Cd2, and Cd3 atoms are bounded together by twelve carboxylate groups of the NTA^{3-} molecules in μ_1–η^1:η^1, μ_2–η^1:η^2, μ_3–η^1:η^2 and μ_2–η^1:η^1 modes, forming a pentanuclear Cd(II) secondary building units (SBUs) (Fig. 1a). In return, the pentanuclear Cd(II) SBUs are linked by NTA^{3-} ligands to form three-dimensional ultramicroporous framework (Fig. 1b and c), where the pore surface is distributed with multiple exposed oxygen active sites from the $Cd_5(COO^-)_{12}$ chain, benefiting for gas adsorption and separation. Topologically, each pentanuclear Cd(II) SBUs is linked by twelve NTA^{3-} ligands, in return, two different NTA^{3-} ligands connect three Cd(II) SBUs respectively, totally, the overall structure is a (3, 3, 12)-connected 3D net with a Schläfli symbol of (4^{16}·6^{36}·8^{14}) (4^2·6)$_2$(4^3)$_2$ (Fig. 1d).

3.2. X-ray power diffraction analyses and thermal analyses

The purity of the sample was verified by assessing the consistency between the measured and simulated values through PXRD analysis. Thermogravimetry analysis results revealed a 7.5 % weight reduction below 100 °C before activation, attributed to the decrease of coordinated water molecules. When the temperature was increased between 100 °C and 200 °C, the weight loss was minimal, suggesting the preservation of structural integrity (Fig. S4) However, above 200 °C, the structure of **1** gradually collapsed. PXRD analysis demonstrated the excellent stability of **1** after immersing in organic solvents (ethanol, methanol, acetonitrile, *N*, *N*-dimethylformamide, dimethyl sulfoxide) and pH 2–11 aqueous solutions for a day (Fig. S5).

3.3. Gas adsorption properties

Structural analysis showed that the pore volume after desolation accounts for 28.4 %. The structure **1** has potential multiple exposed oxygen active sites from the pentanuclear $Cd_5(COO^-)_{12}$ in the pores, indicating its potential to be employed as an adsorbent to separate gases.

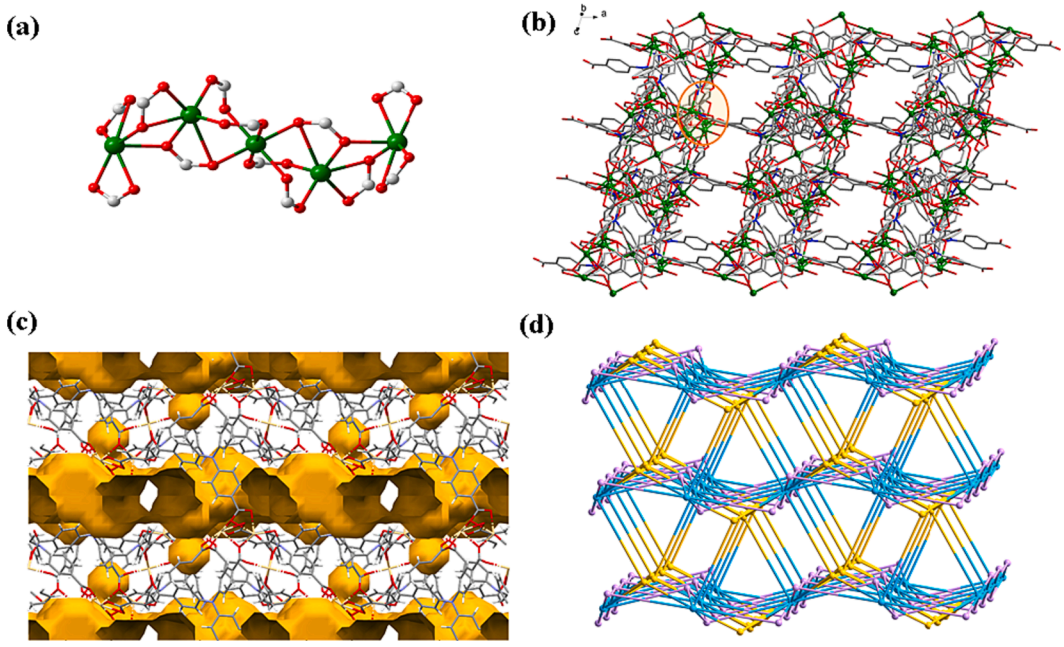

Fig. 1. (a) Cd_5 Cluster node. (b) The three-dimensional stacking along the crystallographic b-axis. (c) Pore structure along the crystallographic *c*-axis. (d) The topological structure of **1**.

Therefore, the performance of **1** in adsorption and separation of the pure component gases was systematically studied.

N_2 adsorption experiments were conducted to analyze the porosity of the activated **1** (**1′**) at 77 K. The N_2 adsorption curve of **1′** exhibited the typical type-I adsorption behavior of microporous materials (Fig. 2a), with the maximum N_2 adsorption capacity reaching 88.1 $cm^3 \cdot g^{-1}$. The Brunauer-Emmett-Teller (BET) method measured that the specific surface area (SSA) was 327.9 $m^2 \cdot g^{-1}$, whereas the Langmuir surface area was 373.5 $m^2 \cdot g^{-1}$. The primary pore size, as obtained from the pore size distribution (PSD) curve, was 4.2 Å (Fig. 2b), in accordance with the pore size measured for the single crystal structure.

To further analyze the permanent porosity and ultramicroporous characteristics of **1′**, we investigated its adsorption capacity for different single-component adsorption curve (CH_4, C_2H_6, C_3H_8) was conducted at 273 and 298 K. The maximum gas uptake capacities of **1′** for single-component adsorption curves (CH_4, C_2H_6, C_3H_8) are 16.4, 71.5, and 67.6 $cm^3 \cdot g^{-1}$, respectively, at 298 K and 100 kPa, with the maximum adsorption capacities at 273 K reaching up to 32.1, 77.5, and 72.7 $cm^3 \cdot g^{-1}$, respectively (Fig. 3). The results showed that the C_3H_8 uptake of **1′** was much steeper than that of C_2H_6 for a low relative pressure, P/P_0, but the uptake of both these compounds was much larger than that of CH_4. This suggested the affinity order of **1′** for guest molecules to be $C_3H_8 > C_2H_6 > CH_4$, which was also confirmed by their adsorption enthalpies (Q_{st}). We know that C_3H_8 has a higher affinity for MOFs and a higher absorption rate than that of C_2H_6 at low pressures. However, due to the large volume of C_3H_8, **1′** can accommodate only a few of these molecules in its limited pore space, resulting in a lower adsorption capacity of **1′** for C_3H_8 (67.6 $cm^3 \cdot g^{-1}$) than that for C_2H_6 (71.5 $cm^3 \cdot g^{-1}$) at 298 K and 100 kPa. The gas occupancy values of **1′** for C_3H_8 and C_2H_6 were 11.98 and 12.68 molecules per unit cell, respectively (Table S3), indicating a much higher filling efficiency compared to CH_4 (2.90 molecules per unit cell). The densities of C_2H_6 and C_3H_8 in **1′** were 0.62 and 0.86 $g \cdot mL^{-1}$, respectively (Table S4), higher than their liquid phase densities at 298 K (0.32 and 0.49 $g \cdot mL^{-1}$, respectively), further demonstrating the dense packing of C_2H_6 and C_3H_8 in **1′** [23]. It is worth mentioning as the testing environment temperature decreased, the adsorption capacity of **1′** for the above gases increased to varying degrees, indicating a physical adsorption behavior [24]. **1′** exhibited

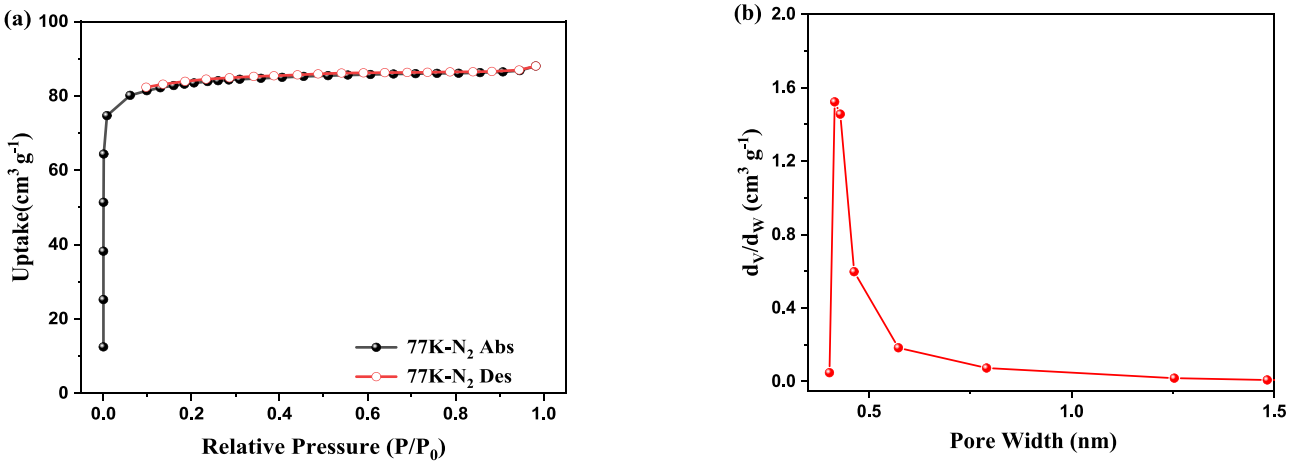

Fig. 2. (a) N_2 adsorption isotherm, and (b) pore size distribution for **1**.

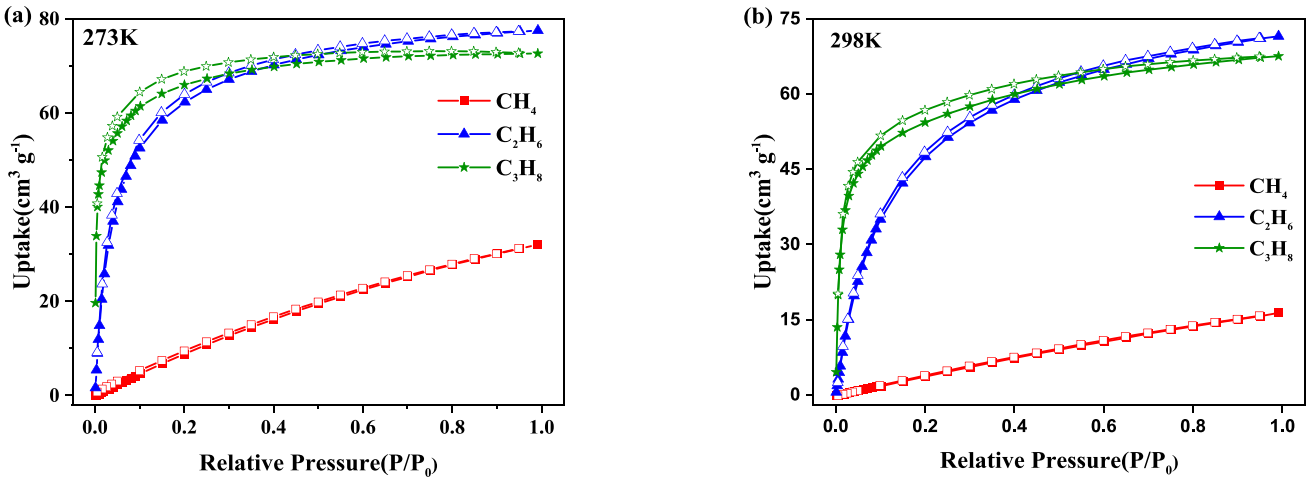

Fig. 3. Adsorption and desorption isotherms of CH_4, C_2H_6, and C_3H_8 for **1′** at (a) 273 K and (b) 298 K.

significant differences in its adsorption capacities for CH_4, C_2H_6, and C_3H_8, further indicating its great potential for CH_4, C_2H_6, and C_3H_8 adsorption and separation.

In addition, the Q_{st} reveal the affinity of the host framework towards the different adsorbates [25–27], playing an important role in the equilibrium separation selectivity of different gases on the material. The Q_{st} of **1′** with coverage change were computed using the Clausius-Clapeyron equation to evaluate the affinity of the above gases with the pore surface. The Q_{st} values of **1′** for CH_4, C_2H_6, and C_3H_8 were determined to be 27.7, 33.3, and 50.5–60.7 $kJ{\cdot}mol^{-1}$, respectively (Fig. 4). Notably, C_3H_8 exhibited a substantially higher Q_{st} throughout the adsorption process compared to C_2H_6 and CH_4, indicating a stronger affinity between the host framework and C_3H_8. It is hypothesized that the extraction of C_3H_8 and C_2H_6 from their mixtures can be achieved with relative ease, as supported by the corresponding adsorption isotherms [28,29].

The above-described significant differences between the **1′** isotherm adsorption curves (Fig. 3) and Q_{st} (Fig. 4) of C_3H_8, C_2H_6, and CH_4 at 273 and 298 K further confirmed the potential of **1′** to separate C_2H_6, C_3H_8, and CH_4 gas mixtures. Therefore, the IAST model was used to predict the equilibrium separation selectivity of CH_4, C_2H_6, and C_3H_8 mixtures by accurately fitting the isotherms to either the dual-site or single-site

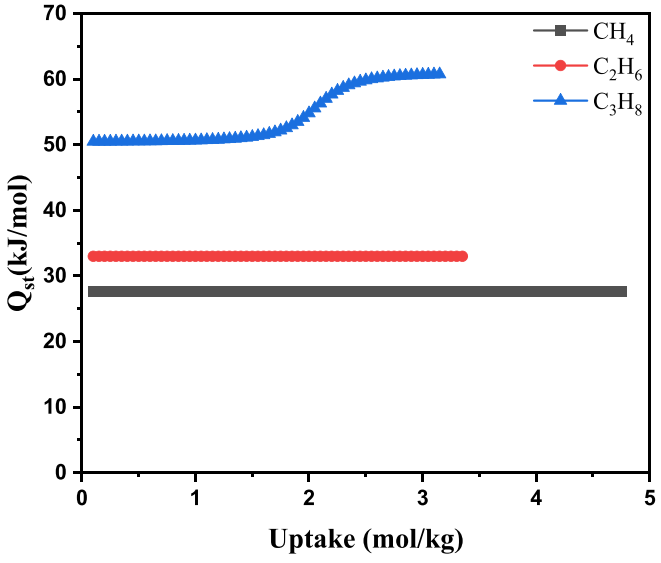

Fig. 4. The adsorption enthalpy (Q_{st}) of **1′** for CH_4, C_2H_6, and C_3H_8 calculated using the corresponding isotherms at 273 and 298 K.

Langmuir-Freundlich/Langmuir equation (detailed parameters are listed in Tables S5–S7 and IAST fitting curves at 273 K and 100 kPa are shown in Fig. 5a). At 298 K and 100 kPa, the theoretical equilibrium separation selectivity of C_2H_6/CH_4 (v/v = 10/85) and C_3H_8/CH_4 (v/v = 5/85) reached 34.3 and 223.8, respectively (Fig. 5b), with the latter value being significantly higher than those of most reported MOFs (Fig. 6d) [14,19,20,30–37]. The separation potential ($\Delta q = (q_{C3H8} + q_{C2H6})\frac{y_{CH4}}{(1-y_{CH4})} - q_{CH4}$) was utilized as a comprehensive indicator to measure both selectivity and capacity [38,39]. The findings indicated that the Δq value for **1′** was 10.77 $mol{\cdot}kg^{-1}$ [Figs. S6-S7], providing further evidence of the effectiveness of separating $CH_4/C_2H_6/C_3H_8$ mixed hydrocarbon gases.

3.4. Breakthrough measurements

To verify the practical $CH_4/C_2H_6/C_3H_8$ separation performance of **1′**, breakthrough experiments were conducted at 298 K. The penetration results of the $CH_4/C_2H_6/C_3H_8$ (v/v/v = 85/10/5) mixture showed in Fig. 6a that CH_4 broke immediately through the packed bed, while C_2H_6 and C_3H_8 were retained for 136 and 280 $min{\cdot}g^{-1}$ (Fig. 6a), respectively, exceeding most previously reported values [40,41]. The CH_4 yield (purity > 99.9 %) was 9.8 $mmol{\cdot}g^{-1}$, surpassing that of most previously reported MOFs [24], lower only in comparison with that of Ni(TMBDC)(DABCO)$_{0.5}$ (13.28 $mmol{\cdot}g^{-1}$) [20] and ZUL-C2 (11.4 $mmol{\cdot}g^{-1}$) [23] (Fig. 6c). It should be noted that the higher "roll-up" peak of C_2H_6 breakthrough curve was due to its smaller Q_{st} compared to C_3H_8, resulting in more significant competitive adsorption of C_3H_8 by **1'**, replacing C_2H_6 [23]. To determine the stability of **1'** in recovering CH_4 from C_2H_6 and C_3H_8 hydrocarbons, the breakthrough tests were repeated five times, each attempt demonstrating consistently exceptional performances (Fig. 6b).

3.5. Molecular simulations

Considering the ability of **1′** to extract highly pure CH_4 from C_2H_6-C_3H_8 hydrocarbons, the adsorption mechanism towards $CH_4/C_2H_6/C_3H_8$ was further investigated. Initially, we employed GCMC simulations (calculated with RASPA) to unveil the favorable CH_4, C_2H_6, and C_3H_8 adsorption sites within the host framework and compute the expected adsorption amounts and gas density distributions (Fig. 7). At 298 K, the GCMC simulated adsorption of CH_4, C_2H_6 and C_3H_8 at pressures ranging from 0 to 100 kPa (Fig. S9). Moreover, the simulated and experimental adsorption at low pressures indicated a marginal variance, which was considered acceptable given the disparities between the two methods. These results validated the accuracy of the force field employed in our

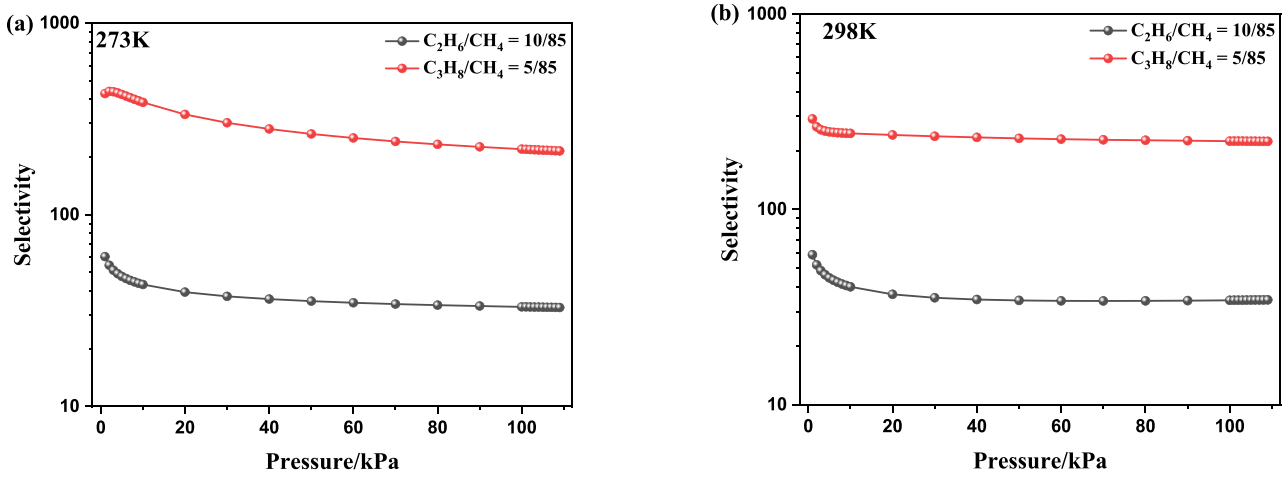

Fig. 5. 1′ selectivity for (a) C_2H_6/CH_4 (v/v = 10/85) and (b) C_3H_8/CH_4 (v/v = 5/85) gas mixtures at 273 and 298 K derived from IAST.

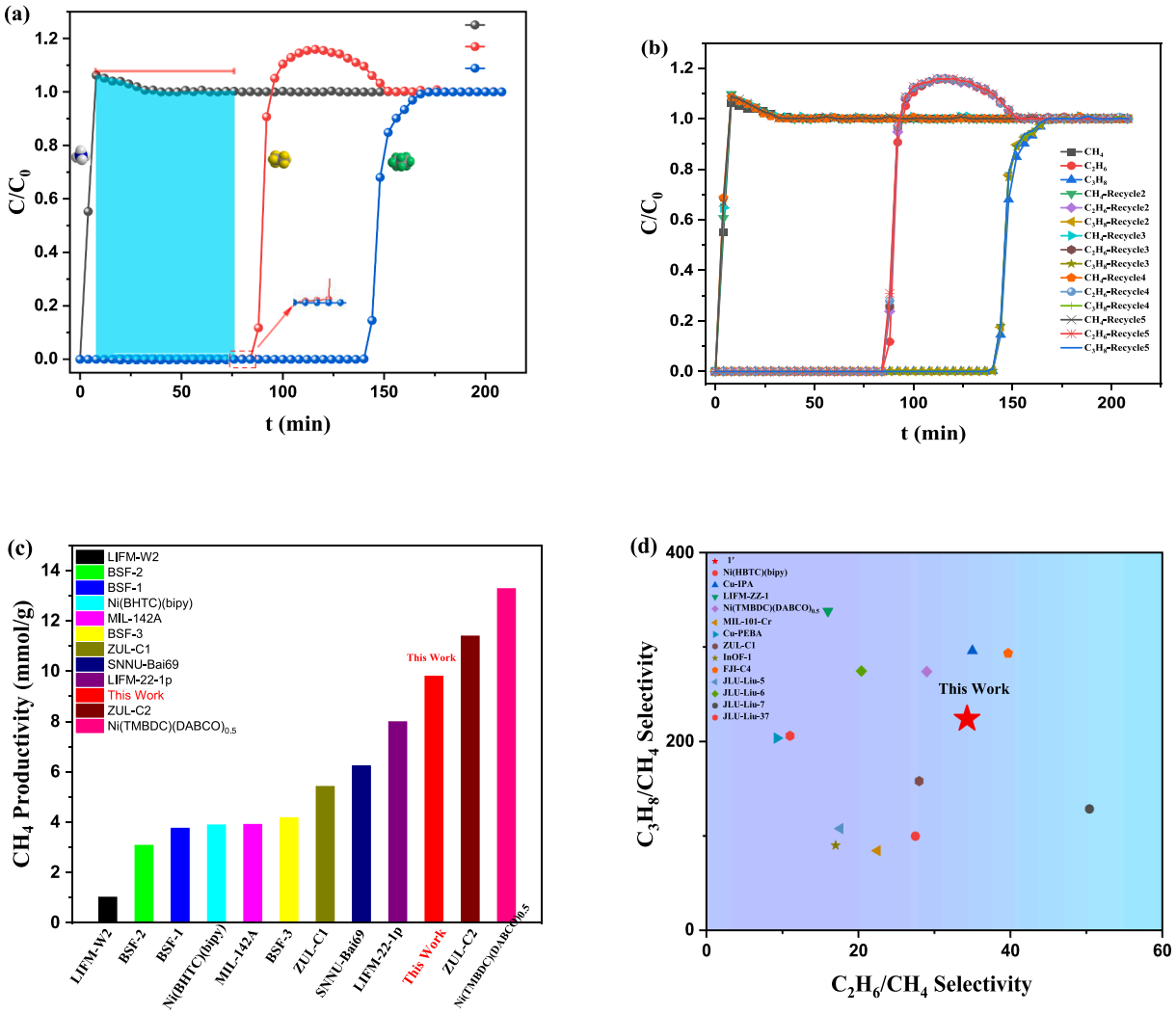

Fig. 6. (a) 1′ breakthrough curves for $CH_4/C_2H_6/C_3H_8$ (v/v/v = 85/10/5) mixtures at 298 K and 100 kPa; (b) 1′ cycling stability test; (c) comparison of high purity CH_4 yield of 1′ with reported benchmark adsorbents for $CH_4/C_2H_6/C_3H_8$ (v/v/v = 85/10/5) mixtures; and (d) comparison of 1′ IAST-computed adsorption selectivity for $CH_4/C_2H_6/C_3H_8$ (v/v/v = 85/10/5) along with previously reported adsorbents at 298 K and 100 kPa.

system. Notably, the experimental adsorption of C_2H_6 by 1′ exceeded that of C_3H_8, which was consistently reproduced by the simulations, further confirming the accuracy of the model. Similarly, we simulated the adsorption capacities of the mixed gases within the host framework by considering a $CH_4/C_2H_6/C_3H_8$ volumetric ratio of 85/10/5 at 298 K and 100 kPa. For separation of $CH_4/C_2H_6/C_3H_8$ (v/v/v = 85/10/5)

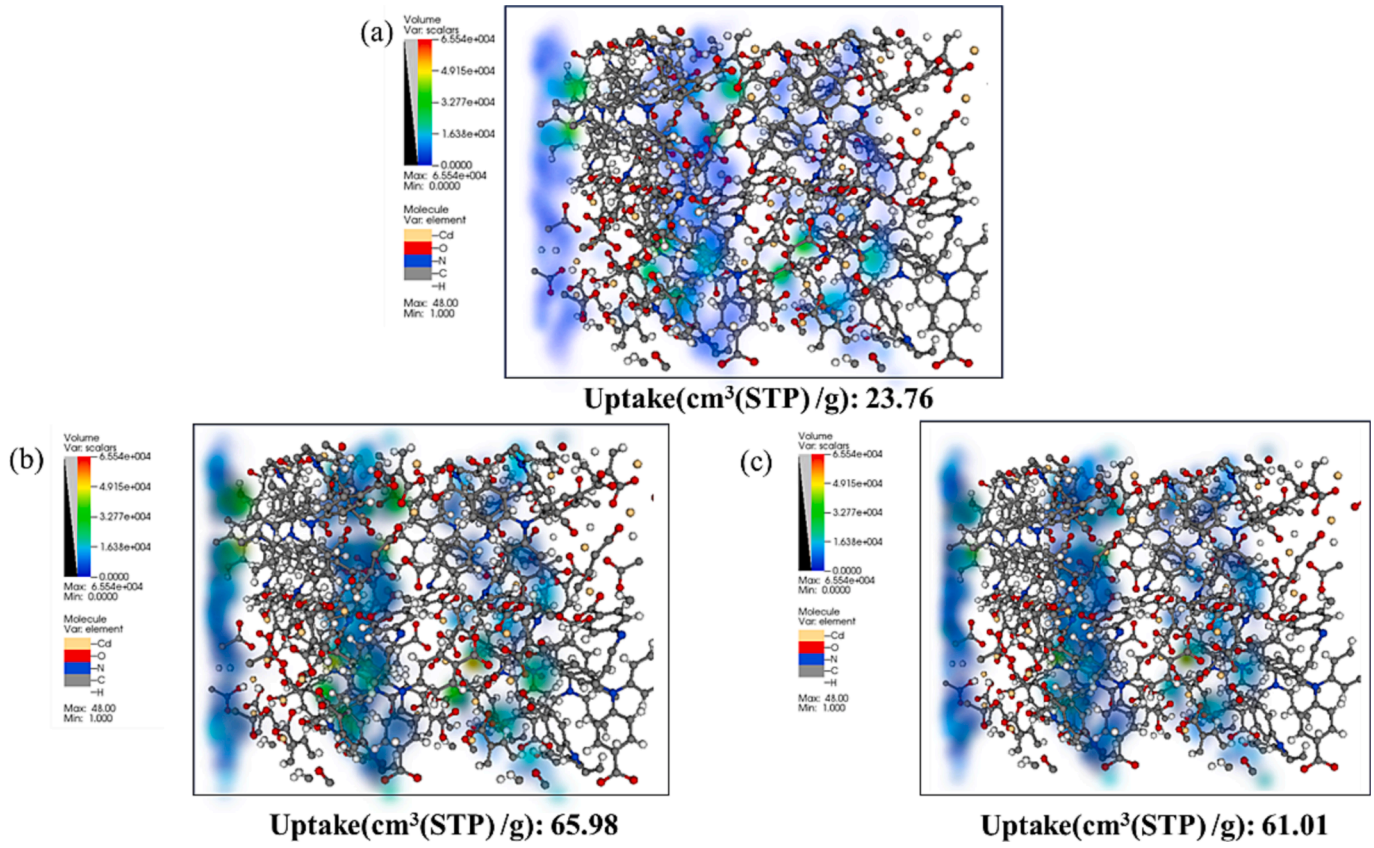

Fig. 7. **1′** density distributions of (a) CH_4, (b) C_2H_6, and (c) C_3H_8 at 298 K and 100 kPa computed from GCMC simulations.

mixtures, the maximum yield of high-purity CH_4 that is theoretically achievable in a fixed bed adsorber is determined by Δq [38,39]. The result of the breakthrough measurement showed a yield of 9.8 mmol·g^{-1}, which was lower than the calculated value of $\Delta q = 12.67$ for **1′** (Fig. S8). The Δq obtained from the adsorbed amount of each component in the IAST was 10.77, which matched the calculated value of $\Delta q = 12.67$, as discussed earlier. The theoretical calculations conducted in this study are in generally accordance with the experimental findings discussed earlier, providing robust validation and reinforcing their coherence.

Therefore, the employed force field model can be considered suitable for capturing the interactions between the host **1′** and the CH_4, C_2H_6, and C_3H_8 adsorbates. Furthermore, the density distributions of CH_4, C_2H_6, and C_3H_8 within the simulated **1′** primarily concentrated in one favorable adsorption region: the oxygen sites within the Cd_5(II) clusters in the channel, where these molecules are prone to adsorption [42]. The adsorption density of C_2H_6 surpassed that of C_3H_8 and CH_4 at 100 kPa and 298 K, consistent with the static adsorption curves and simulation results (Fig. 7).

Based on the approximate adsorption sites obtained from the DFT (calculated with CP2K) calculations, we selected structural fragments near the NTA^{3-} ligand and Cd_5(II) clusters as the initial target adsorption sites, which were further subjected to CP2K calculations. This approach provides a more detailed demonstration of the interactions between the gas molecules and host-framework. Multiple-site interactions were observed for the CH_4, C_2H_6, and C_3H_8 molecules, including (i) C–H•••O interactions with carboxylic O atoms on neighboring Cd_5(II) clusters and (ii) C–H interactions with C atoms on the benzene ring via van der Waals forces. Particularly, the interaction of the Cd_5(II) O-sites with C_3H_8 (1.71–2.26 Å) was stronger than that with C_2H_6 (2.20–3.40 Å). Moreover, despite the multi-point interactions with **1′**, C_3H_8 (-62.1 kJ·mol^{-1}) exhibited a lower calculated value of the binding energy between gas molecules and the framework than C_2H_6 (-55.4 kJ·mol^{-1}). The calculated binding energies (C_2H_6), while slightly higher than the experimental Q_{st} values, remain reasonable given the inherent limitations of theoretical calculation [43,44]. These computational simulations thoroughly confirmed the strong adsorption affinity of **1′** for C_3H_8. However, the final adsorption capacity **1′** for C_3H_8 did not exceed that for C_2H_6 due to the pore size limitation in the skeletal structure (See Fig. 8).

4. Conclusion

In summary, a stable ultramicroporous Cd(II)-MOF, with multiple exposed active oxygen sites from the $Cd_5(COO^-)_{12}$ chain on the pore surface has been constructed to exhibit high adsorption capacity for C_2H_6 and C_3H_8 hydrocarbons. The gas adsorption and separation performance analysis showed that the gas selectivity separation rate of **1′** for C_2H_6/CH_4 and C_3H_8/CH_4 was 34.3 and 223.8, respectively. Dynamic breakthrough experiments comprehensively confirmed the promising potential of **1′** as an adsorbent for practical $CH_4/C_2H_6/C_3H_8$ separation with a high-purity (>99.9 %) CH_4 yield of 9.8 mmol·g^{-1}. Furthermore, GCMC simulations and DFT calculations reveal that the high capture and selectivity of **1′** for C_3H_8 and C_2H_6 can be attributed to the abundant oxygen sites present in the channels.

CRediT authorship contribution statement

Xing-Zhe Guo: Investigation, Software, Writing – original draft. **Bingwen Li:** . **Guang-Zu Xiong:** Funding acquisition, Investigation, Software, Validation, Visualization. **Bing Lin:** Investigation, Software, Validation. **Liu-Cheng Gui:** Software. **Xiao-Xia Zhang:** Supervision. **Zhihui Qiu:** Supervision. **Rajamani Krishna:** Methodology. **Xinfang Wang:** Supervision. **Xin Yan:** Conceptualization. **Shui-Sheng Chen:**

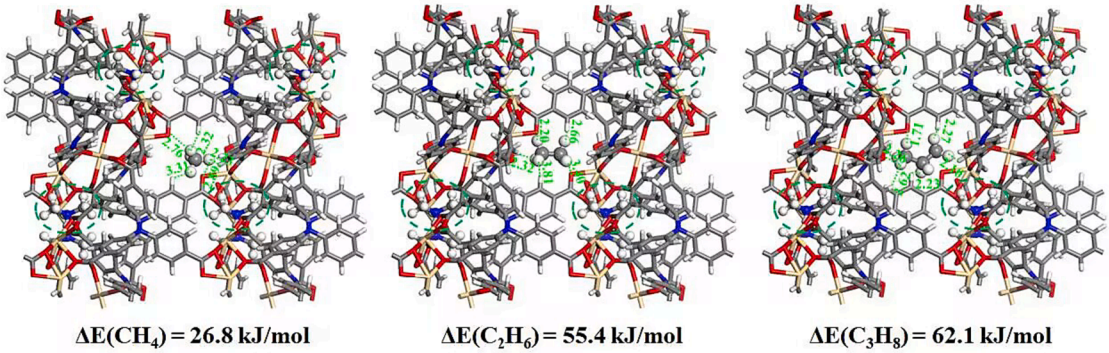

Fig. 8. DFT calculated accessible adsorption O-sites for (a) CH_4@**1**′, (b) C_2H_6@**1**′, and (c) C_3H_8@**1**′. The $[(Me)_2NH_2]^+$ cations in the host framework are highlighted by the green circles. (For interpretation of the references to colour in this figure legend, the reader is referred to the web version of this article.)

Conceptualization, Project administration.

Declaration of competing interest

The authors declare that they have no known competing financial interests or personal relationships that could have appeared to influence the work reported in this paper.

Data availability

Data will be made available on request.

Acknowledgment

This work was supported by the Natural Science Foundation of Shandong Province (ZR2021QB159 and ZR202103040556), the National Natural Science Foundation of China (21401099), the National Natural Science Foundation of Anhui Province (2008085MB32 and KJ2021ZD73). This work is also supported by the Talent Program Foundation of Dezhou University (2021xjrc102).

Appendix A. Supplementary material

Supplementary data to this article can be found online at https://doi.org/10.1016/j.seppur.2023.125987.

References

[1] S. Koen, R.-T. Rodrigo, V. Geert, Z. Bob, Historical variation in the capital costs of natural gas, carbon dioxide and hydrogen pipelines and implications for future infrastructure, Int. J. Greenh. Gas Con. 5 (2011) 1614–1623.
[2] Z.B. Bao, G.G. Chang, H.B. Xing, K. Rajamani, Q.L. Ren, B.L. Chen, Potential of microporous metal–organic frameworks for separation of hydrocarbon mixtures, Energy Environ. Sci. 9 (2016) 3612–3641.
[3] C. Cong, Y.M. Deng, D. Raf, B. Jan, X.F. Fan, Post-combustion carbon capture, Renew. Sust. Energy Rev. 138 (2021), 110490.
[4] Y.S. Liu, N.Q. Sun, Z.Y. Li, P. Xiao, Y. Xing, X. Yang, C.Y. Zhao, C.Z. Zhang, H. Y. Wang, T.Y. Ralph, A.W. Paul, Recovery of high-purity NO_2 and SO_2 products from iron-ore sintering flue gas by distillation: process design, optimization and analysis, Sep. Purif. Technol. 264 (2021), 118308.
[5] W. Haryo, S. Herri, G. Nurak, H. Dwi, Y. Kunio, H. Qun, M. Yan, Recent developments of deep eutectic solvent as absorbent for CO_2 removal from syngas produced from gasification: current status, challenges, and further research, J. Environ. Chem. Eng. 9 (2021), 105439.
[6] A. Olajumobi, L. Wang, W.G. Xie, D. Richard, A. Malek, T. Sam, Post-combustion CO_2 capture via a variety of temperature ranges and material adsorption process: a review, J. Environ. Manage. 313 (2022), 115026.
[7] Y.J. Jiang, J.B. Hu, L.Y. Wang, W.Q. Sun, N. Xu, K. Rajamani, D. Simon, X.L. Xi, H. B. Xing, Y.B. Zhang, Comprehensive pore tuning in an ultrastable fluorinated anion cross-linked cage-like MOF for simultaneous benchmark propyne recovery and propylene purification, Angew. Chem. Int. Edit. 61 (2022), e202200947.
[8] J. Wang, Y. Zhang, Y. Su, X. Liu, P.X. Zhang, R.B. Lin, S.X. Chen, Q. Deng, Z. L. Zeng, S.G. Deng, B.L. Chen, Fine pore engineering in a series of isoreticular metal-organic frameworks for efficient C_2H_2/CO_2 separation, Nat. Commun. 13 (2022) 200.
[9] B.Y. Zhu, J.W. Cao, M. Soumya, P. Tony, T. Zhang, T. Wang, X. Jiang, A. F. Katherine, J.Z. Michael, K.J. Chen, Pore engineering for one-step ethylene purification from a three-component hydrocarbon mixture, J. Am. Chem. Soc. 143 (2021) 1485–1492.
[10] F. Zheng, L.D. Guo, B.X. Gao, L.Y. Li, Z.G. Zhang, Y.W. Yang, Y.W. Yang, B.G. Su, Q. L. Ren, Z.B. Bao, Engineering the pore size of pillared-layer coordination polymers enables highly efficient adsorption separation of acetylene from ethylene, ACS Appl. Mater. Inter. 11 (2019) 28197–28204.
[11] Y.B. Zhang, L.F. Yang, L.Y. Wang, D. Simon, H.B. Xing, H., A microporous metal-organic framework supramolecularly assembled from a Cu II dodecaborate cluster complex for selective gas separation, Angew. Chem. Int. Edit. 131 (2019) 8229–8234.
[12] Y.B. Zhang, L.F. Yang, L.Y. Wang, X.L. Cui, H.B. Xing, Pillar iodination in functional boron cage hybrid supramolecular frameworks for high performance separation of light hydrocarbons, J. Mater. Chem. A 7 (2019) 27560–27566.
[13] W.Q. Sun, J.B. Hu, D. Simon, L.Y. Wang, K. Rajamani, Y.B. Zhang, Highly selective gas separation by two isostructural boron cluster pillared MOFs, Sep. Purif. Technol. 283 (2022), 120220.
[14] Z. Zeng, W. Wang, X.H. Xiong, N.X. Zhu, Y.Y. Xiong, Z.W. Wei, J.J. Jiang, Flexible microporous copper (II) metal–organic framework toward the storage and separation of C1–C3 hydrocarbons in natural gas, Inorg. Chem. 60 (2021) 8456–8460.
[15] L. Anna, K. Konstantin, N. Anton, D. Danil, F. Vladimir, Efficient separation of methane, ethane, and propane on mesoporous metal-organic frameworks, Chem. Eng. J. 453 (2023), 139642.
[16] B. Eirc, Q. Wendy, K. Rajamani, Z. Joseph, B. Craig, L. Jeffrey, Hydrocarbon separations in a metal–organic framework with open iron (II) coordination sites, Science 335 (2012) 1606–1610.
[17] K.P. Yadava, B. Bhaskarjyoti, Separation of methane from ethane and propane by selective adsorption and diffusion in MOF Cu-BTC: a molecular simulation study, J. Mol. Graph. Model. 97 (2020), 107574.
[18] L. Wang, W.H. Zhang, J. Ding, L.L. Gong, K. Rajamani, Y.Y. Ran, L. Chen, F. Luo, Th-MOF showing six-fold imide-sealed pockets for middle-size-separation of propane from natural gas, Nano Res. 16 (2023) 3287–3293.
[19] D.X. Lin, S. Tu, L. Yu, Y.N. Yuan, Y. Wu, X. Zhou, Z. Li, Q.B. Xia, Highly efficient separation of $CH_4/C_2H_6/C_3H_8$ from natural gas on a novel copper-based metal–organic framework, Ind. Eng. Chem. Res. 62 (2023) 5252–5261.
[20] Y.F. Wu, Z.W. Liu, J.J. Peng, X. Wang, X. Zhou, Z. Li, Enhancing selective adsorption in a robust pillared-layer metal–organic framework via channel methylation for the recovery of C2–C3 from natural gas, ACS Appl. Mater. Inter. 12 (2020) 51499–51505.
[21] X.X. Zhang, X.Z. Guo, S.S. Chen, H.W. Kang, Y. Zhao, J.X. Gao, G.Z. Xiong, L. Hou, A stable microporous framework with multiple accessible adsorption sites for high-capacity adsorption and efficient separation of light hydrocarbons, Chem. Eng. J. 466 (2023), 143170.
[22] Y. Shen, X.F. Yang, H.B. Zhu, Y. Zhao, W.S. Li, A unique 3D metal–organic framework based on a 12-connected pentanuclear Cd(II) cluster exhibiting proton conduction, Dalton Trans. 44 (2015) 14741–14746.
[23] J.Y. Zhou, T. Ke, S. Felix, S. Norbert, Z.G. Zhang, Z.B. Bao, X. He, Q.L. Ren, Q. W. Yang, Tunable confined aliphatic pore environment in robust metal-organic frameworks for efficient separation of gases with a similar structure, J. Am. Chem. Soc. 144 (2022) 14322–14329.
[24] M.J. Zhang, Z. Gong, Z.H. Tan, H. Liu, M.X. Yang, Study on heat adsorption based on the experiment of coal adsorption of methane by using the weight method, J. Natural Gas Geosci. 6 (2021) 245–253.
[25] S.M. Wang, M. Shivanna, Q.Y. Yang, Nickel-based metal–organic frameworks for coal-bed methane purification with record CH_4/N_2 selectivity, Angew. Chem. Int. Edit. 61 (2022), e202201017.
[26] F. Zheng, L.H. Chen, R.D. Chen, Z.G. Zhang, Q.W. Yang, Y.W. Yang, B.G. Su, Q. L. Ren, Z.B. Bao, A robust two–dimensional layered metal–organic framework for efficient separation of methane from nitrogen, Sep. Purif. Technol. 281 (2022), 119911.

[27] Q. Zhang, L. Zhou, P.X. Liu, L.B. Li, S.Q. Yang, Z.F. Li, T.L. Hu, Integrating tri-mural nanotraps into a microporous metal-organic framework for C_2H_2/CO_2 and C_2H_2/C_2H_4 separation, Sep. Purif. Technol. 296 (2022), 121404.
[28] S.S. Jiang, J.Q. Li, M. Feng, R.D. Chen, L.D. Guo, Q.Q. Xu, L.H. Chen, F.X. Shen, Z. G. Zhang, Y.W. Yang, Q.L. Ren, Q.W. Yang, Z.B. Bao, Hydrophobic paraffin-selective pillared-layer MOFs for olefin purification, J. Mater. Chem. A 10 (2022) 24127–24136.
[29] Q. Zhang, X. Lian, K. Rajamani, S.Q. Yang, T.L. Hu, An ultramicroporous metal-organic framework based on octahedral-like cages showing high-selective methane purification from a six-component C1/C2/C3 hydrocarbons mixture, Sep. Purif. Technol. 304 (2023), 122312.
[30] P.T. Guo, M. Chang, T.A. Yan, Y.X. Li, D.H. Liu, A pillared-layer metal-organic framework for efficient separation of $C_3H_8/C_2H_6/CH_4$ in natural gas, Chin. J. Chem. Eng. 42 (2022) 10–16.
[31] L.Z. Qin, X.H. Xiong, S.H. Wang, L. Zhang, L.L. Meng, L. Yan, Y.N. Fan, T.A. Yan, D. H. Liu, Z.W. Wei, C.Y. Su, MIL-101-Cr/Fe/Fe-NH_2 for efficient separation of CH_4 and C_3H_8 from simulated natural gas, ACS Appl. Mater. Inter. 14 (2022) 45444–45450.
[32] S.M. Wang, Q.Y. Yang, A copper-based metal-organic framework for upgrading natural gas through the recovery of C_2H_6 and C_3H_8, GreenChE. 4 (2023) 81–87.
[33] Y.W. Chen, Z.W. Qiao, D.F. Lv, H.X. Wu, R.F. Shi, Q.B. Xia, H.H. Wang, J. Zhou, Z. Li, Selective adsorption of light alkanes on a highly robust indium-based metal–organic framework, Ind. Eng. Chem. Res. 56 (2017) 4488–4495.
[34] L. Li, X.S. Wang, J. Liang, Y.B. Huang, H.F. Li, Z.J. Lin, R. Rong, Water-stable anionic metal–organic framework for highly selective separation of methane from natural gas and pyrolysis gas, ACS Appl. Mater. Inter. 8 (2016) 9777–9781.
[35] D.M. Wang, T.T. Zhao, Y. Cao, S. Yao, G.H. Li, Q.S. Huo, Y.L. Liu, High-performance gas adsorption and separation of natural gas in two microporous metal–organic frameworks with ternary building units, Chem. Commun. 50 (2014) 8648–8650.
[36] J.H. Luo, J. Wang, Y. Cao, S. Yao, L.R. Zhang, Q.S. Huo, Y.L. Liu, Assembly of an indium–porphyrin framework JLU-Liu7: a mesoporous metal–organic framework with high gas adsorption and separation of light hydrocarbons, Inorg. Chem. Front. 4 (2017) 139–143.
[37] J.T. Li, X.L. Luo, N. Zhao, L.R. Zhang, Q.S. Huo, Y.L. Liu, Two finite binuclear [M_2(μ_2-OH) $(COO)_2$](M= Co, Ni) based highly porous metal–organic frameworks with high performance for gas sorption and separation, Inorg. Chem. 56 (2017) 4141–4147.
[38] R. Krishna, Screening Metal-Organic Frameworks for mixture separations in fixed-bed adsorbers using a combined selectivity/capacity metric, RSC Adv. 7 (2017) 35724–35737.
[39] R. Krishna, Metrics for evaluation and screening of metal-organic frameworks for applications in mixture separations, ACS Omega 5 (2020) 16987–17004.
[40] Q.B. Dai, W.W. Liang, Z.W. Liu, F. Xu, Q.B. Xia, X. Zhou, J. Xiao, Z. Li, Novel granular biomass-based carbons with excellent C_2H_6/CH_4 selectivity for recovering light hydrocarbons from natural gas, ACS Sustain. Chem. Eng. 10 (2022) 5633–5642.
[41] Y.F. Zhang, H.Y. Xiao, X. Zhou, X. Wang, Z. Zhong, Selective adsorption performances of UiO-67 for separation of light hydrocarbons C1, C2, and C3, Ind. Eng. Chem. Res. 56 (2017) 8689–8696.
[42] Y. Zhang, X.Y. Deng, X.R. Li, X. Liu, P.X. Zhang, L.H. Chen, Z.H. Yan, J. Wang, S. G. Deng, A stable metal-organic framework with oxygen site for efficiently trapping acetylene from acetylene-containing mixtures, Sep. Purif. Technol. 316 (2023), 123751.
[43] L. Zhao, P.X. Liu, C.H. Deng, T. Wang, S. Wang, Y.J. Tian, J.S. Zou, X.C. Wu, Y. Zhang, Y.L. Peng, Z.J. Zhang, M.J. Zaworotko, Robust ultra-microporous metal-organic frameworks for highly efficient natural gas purification, Nano Res. 16 (2023) 12338–12344.
[44] Y.X. Ye, Y. Xie, Y.S. Shi, L.S. Gong, J. Phipps, A.M. Al-Enizi, A. Nafady, B.L. Chen, S.Q. Ma, A microporous metal-organic framework with unique aromatic pore surfaces for high performance C_2H_6/C_2H_4 separation, Angew. Chem. Int. Edit. 62 (2023) e202302564.

Electronic supplementary information (ESI)

A stable ultramicroporous Cd(II)-MOF with accessible oxygen sites for efficient separation of light hydrocarbons with high methane production

Xing-Zhe Guo [a, b §], Bingwen Li [a §*], Guang-Zu Xiong [b §], Bing Lin [c], Liu-Cheng Gui [c], Xiao-Xia Zhang [b], Zhihui Qiu [c], Rajamani Krishna [d], Xinfang Wang [a], Xin Yan [a*], Shui-Sheng Chen [b*]

[a] *Shandong Key Laboratory of Biophysics, Institute of Biophysics, Dezhou University, Dezhou, 253023, China*

[b] *Engineering Research Center of Oligosaccharides, Fuyang Normal University, Fuyang, 236041, China*

[c] *School of Chemistry & Pharmaceutical Sciences, Guangxi Normal University, Guilin, Guangxi, 541004, China*

[d] *Van't Hoff Institute for Molecular Sciences, University of Amsterdam, The Netherlands*

* E-mail addresses: libingwen@dzu.edu.cn, yanxin2012@iccas.ac.cn, chenss@fynu.edu.cn.

Phone: +86-05582595836.

§ Equal contribution

Content of Table

Materials and methods

All chemical reagents are commercially available without further purification. IR spectra were measured on a Thermo Fisher IS-50 FT-IR Spectrometer in the range of 400-4000 cm^{-1}. Elemental analyses were carried out on a Vario MACRO cube elemental analyzer. TGA was measured from 25 to 800 ºC on a TA Instrument at a heating rate 10 ºC/min under air atmosphere. X-ray powder diffractions of titled complexes were measured on a Rigaku XtaLAB Synergy PC diffractometer with Cu-Kα radiation over the 2θ range of 5-50° at room temperature. All gas adsorption isotherms were measured on a Quantachrome Autosorb-iQ surface area by the static volume method.

Crystal data collection and refinement

Single-crystal X-ray diffraction data for **1** were collected on Bruker SMART APEX II with Mo Kα radiation (λ = 0.71073 Å) using the ω -φ scan mode at 293 K. The SAINT programs were used for empirical absorption corrections and data integration [1]. All Crystal structures were solved by direct method and refined by full-matrix least-squares refinements within the ShelXS-2014 and ShelXL-2014 program [2]. All non-hydrogen atoms were refined anisotropically. Hydrogen atoms of the organic ligands were in the geometrically ideal positions and refined using a riding model. The details of the crystal parameters and selected bond lengths and angles are listed in Table S1 and Table S2.

Calculation details

Fitting of experimental data on pure component isotherms for calculating IAST selectivity

The experimental isotherm data for pure CH_4, C_2H_6 were fitted using a single-site Langmuir-Freundlich (L-F) model:

$$q = q_{A,sat}\frac{b_A p^{v_A}}{1 + b_A p^{v_A}} \quad \text{(S1)}$$

The experimental isotherm data for pure C_3H_8 were fitted using a dual-site Langmuir-Freundlich (L-F) model:

$$q = q_{A,sat}\frac{b_A p^{v_A}}{1 + b_A p^{v_A}} + q_{B,sat}\frac{b_B p^{v_B}}{1 + b_B p^{v_B}} \quad \text{(S2)}$$

Here, P is the pressure of the bulk gas at equilibrium with the adsorbed phase (kPa), q is the adsorbed amount per mass of adsorbent (mol kg^{-1}), $q_{A,sat}$ and $q_{B,sat}$ are the saturation capacities of site A and B (mol kg^{-1}), b_A and b_B are the affinity coefficients of site A and B (kPa^{-1}), and v_A and v_B represent the deviations from an ideal homogeneous surface.

Fitting of experimental data on pure component isotherms for calculating Q_{st}

The unary isotherms for C_3H_8 measured at two different temperatures 273 K, and 298 K in Cd-MOF were fitted with excellent accuracy using the dual-site Langmuir model, where we distinguish two distinct adsorption sites A and B:

$$q = \frac{q_{sat,A} b_A p}{1 + b_A p} + \frac{q_{sat,B} b_B p}{1 + b_B p} \quad \text{(S3)}$$

In eq (S3), the Langmuir parameters b_A, b_B are both temperature dependent

$$b_A = b_{A0}\, exp\left(\frac{E_A}{RT}\right);\ b_B = b_{B0}\, exp\left(\frac{E_B}{RT}\right) \quad \text{(S4)}$$

In eq (S4), E_A, E_B are the energy parameters associated with sites A, and B, respectively.

The unary isotherms for CH_4, and C_2H_6 measured at two different temperatures 273 K, and 298 K in Cd-MOF were fitted with excellent accuracy using the single-site Langmuir model.

The unary isotherm fit parameters are provided in Table S7.

Calculation of isosteric heat of adsorption (Q_{st})

The isosteric heat of adsorption, Q_{st}, is defined as

$$Q_{st} = -RT^2\left(\frac{\partial\, ln\, p}{\partial T}\right)_q \quad \text{(S5)}$$

where, the derivative in the right member of eq (S5) is determined at constant adsorbate loading, q. the derivative was determined by analytic differentiation of the combination of eq (S3), eq (S4), and eq (S5).

Separation potential

For separation of 5/10/85 $C_3H_8/C_2H_6/CH_4$ mixtures, the maximum productivity of purified CH_4 that is theoretically achievable in a fixed bed adsorber is determined by the metric defined by Krishna [3, 4] as the **separation potential**, Δq, derived on the basis of the shock wave model:

$$\Delta q = (q_{C3H8} + q_{C2H6})\frac{y_{CH4}}{(1 - y_{CH4})} - q_{CH4} \quad \text{(S6)}$$

In eq (S6), y_{CH4} is the methane mole fractions of the feed mixture during the adsorption cycle. In the derivation of eq (S6), it is assumed that the concentration "fronts" traversed the column in the form of shock waves during the desorption cycle. The molar loadings $q_{C3H8}, q_{C2H6}, q_{CH4}$ of the three components are determined using the Ideal Adsorbed Solution Theory (IAST) of Myers and Prausnitz using the unary isotherm fits in as data inputs.[5] At a total pressure of 100 kPa, the value of Δq is 10.77 mol kg^{-1}.

Prediction of Adsorption Selectivity via IAST

The adsorption selectivity for separation of C_3H_8, C_2H_6, CH_4 is defined by

$$\text{S7: } S_{ads} = \frac{q_1/q_2}{p_1/p_2}$$

where q_1, q_2 are the molar loading (units: mol kg^{-1}) of C_3H_8/C_2H_6 and CH_4 in the adsorbed phase in equilibrium with a gas mixture with partial pressures p_1, p_2 in the bulk gas.

Notation

b	Langmuir constant, Pa^{-1}
E	energy parameter, J mol^{-1}
q	component molar loading of species i, mol kg^{-1}
q_{sat}	saturation loading, mol kg^{-1}
Δq	separation potential, mol kg^{-1}
Q_{st}	isosteric heat of adsorption, J mol^{-1}
T	absolute temperature, K

Breakthrough experiment

The breakthrough experiments of light hydrocarbons were carried out in a dynamic gas breakthrough equipment. All experiments were conducted using a stainless-steel column (4.6

mm inner diameter × 30 mm). According to the different particle size and Table S2 density of **1** sample powder, the weight packed in the column was: **1** (0.500 g), respectively. The columns packed with sample were firstly purged with N_2 flow (15 ml·min^{-1}) for 24 h at 298 K. The ternary mixed gas of $C_3H_8/C_2H_6/CH_4$=5/10/85 (v/v/v) was then introduced at 2.0 ml min $^{-1}$, respectively. Outlet gas from the column was monitored using gas chromatography (GC-2010 pro, SHIMADZU) with a flame ionization detector (FID). When the breakthrough experiments were finished, the column was heated to 323 K and a flow rate of 4~6 ml·min^{-1} N_2 was introduced, and the outlet gas from the column was also monitored.

Calculation of gas occupancy and gas density

Gas occupancy for CH_4, C_2H_6, and C_3H_8 in **1** were calculated by the following equation:

$$\text{Gas occupancy} = Q * N_A * \rho * V_c * 10^{-27}$$

Here, Q (mmol/g) is the saturated gas uptake; N_A is the Avogadro constant; ρ(g/cm^3) is the structure density and V_c (Å3) is the cell volume. Calculated results are shown in Table S3.

Gas density of CH_4, C_2H_6, and C_3H_8 in the pore of **1** were calculated by the following equation:

$$\text{Gas density} = Q * 10^{-3} * M/V_p$$

Here, Q (mmol/g) is the saturated gas uptake; M is the molar mass (g/mol) and V_p (ml/g) is the pore volume. The calculated results are shown in Table S4.

Density-functional theory (DFT) and GCMC calculations

DFT calculations were carried out using the CP2K code. A mixed Gaussian and planewave basis sets were employed to the calculations. Core electrons were represented with norm-conserving Goedecker-Teter-Hutter pseudopotentials, and the valence electron wavefunction was expanded in a double-zeta basis set with polarization functions along with an auxiliary plane wave basis set with an energy cutoff of 400 Ry. The generalized gradient approximation exchange-correlation functional of Perdew, Burke, and Enzerhof (PBE) was used. Each configuration was optimized with the Broyden-Fletcher-Goldfarb-Shanno (BGFS) algorithm with SCF convergence criteria of 3×10^{-6} au. To compensate the long-range van der Waals dispersion interaction between the adsorbate and the zeolite, the DFT-D3 scheme with an empirical damped potential term was added into the energies obtained from exchange-correlation functional in all calculations. The supercell of **1** was modeled using 2 × 1 × 1 unit cell.

To calculate adsorption performance in MOF, we use the GCMC simulation method within RASPA package [6]. During the simulation, the MOF are treated as rigid framework and the

GenericMOFs force field is used [7]. As for the gas molecules, the potential parameters are taken from TraPPE force field. A cutoff distance is set to 12 Å for the Lennard-Jones (LJ) interactions, and all unit cells were sufficiently replicated to avoid interaction between periodic replica. The long-range electrostatic interactions are treated with CoulombSmoothed algorithm. For each state point, GCMC simulations consist of 100000 steps to ensure the equilibration, followed by 100000 steps to sample the desired thermodynamic properties.

Table S1 Selected bond lengths [Å] and bond angles [º] for **1**.

Cd1-O7	2.2856(19)	Cd3-O13	2.246(3)
Cd1-O7^{1}	2.286(2)	O12-Cd2^{8}	2.2406(19)
Cd1-O5^{1}	2.2181(19)	O12-Cd3^{9}	2.394(2)
Cd1-O5	2.2181(19)	O10-Cd2^{10}	2.579(2)
Cd1-O11^{2}	2.2754(19)	O10-Cd3^{11}	2.314(2)
Cd1-O11^{3}	2.2754(19)	O3-Cd3^{12}	2.329(2)
Cd2-O12^{3}	2.2406(19)	O4-Cd3^{12}	2.460(2)
Cd2-O6	2.251(2)	O9-Cd2^{10}	2.298(2)
Cd2-O10^{4}	2.579(2)	Cd3-O3^{7}	2.329(2)
Cd2-O8	2.168(2)	Cd3-O4^{7}	2.460(2)
Cd2-O9^{4}	2.298(2)	Cd3-O2	2.308(3)
Cd3-O12^{5}	2.394(2)	Cd3-C36^{7}	2.745(3)
Cd3-O10^{6}	2.314(2)	Cd3-O1	2.573(3)
O7-Cd1-O7^{1}	180.0	O8-Cd2-O12^{3}	119.59(9)
O5-Cd1-O7	91.03(8)	O8-Cd2-O6	103.32(9)
O5-Cd1-O7^{1}	88.97(8)	O8-Cd2-O10^{4}	139.86(8)
O51-Cd1-O7^{1}	91.03(8)	O8-Cd2-O9^{4}	90.16(9)
O51-Cd1-O7	88.97(8)	O9^{4}-Cd2-O10^{4}	53.26(8)
O5-Cd1-O5^{1}	180.0	O12^{5}-Cd3-O4^{6}	78.18(8)
O5-Cd1-O11^{2}	91.01(7)	O12^{5}-Cd3-O1	67.96(10)
O51-Cd1-O11^{3}	91.01(7)	O10^{7}-Cd3-O12^{5}	79.07(7)
O5-Cd1-O11^{3}	88.99(7)	O10^{7}-Cd3-O3^{6}	136.54(8)
O51-Cd1-O11^{2}	88.99(7)	O10^{7}-Cd3-O4^{6}	85.62(8)
O11^{2}-Cd1-O7^{1}	90.05(8)	O10^{7}-Cd3-O1	80.20(10)
O11^{3}-Cd1-O7	90.05(8)	O3^{6}-Cd3-O12^{5}	104.53(8)
O11^{2}-Cd1-O7	89.95(8)	O3^{6}-Cd3-O4^{6}	54.17(8)
O11^{3}-Cd1-O7^{1}	89.95(8)	O3^{6}-Cd3-O1	142.05(9)
O11^{2}-Cd1-O11^{3}	180.0	O4^{6}-Cd3-O1	145.13(11)
O12^{3}-Cd2-O6	124.17(9)	O2-Cd3-O12^{5}	83.26(10)
O12^{3}-Cd2-O10^{4}	76.57(7)	O2-Cd3-O10^{7}	134.03(11)

O12[3]-Cd2-O9[4]	121.77(8)	O2-Cd3-O3[6]	88.90(11)
O6-Cd2-O10[4]	93.40(7)	O2-Cd3-O4[6]	131.43(10)
O6-Cd2-O9[4]	89.64(9)	O2-Cd3-O1	53.83(12)
O13-Cd3-O12[5]	164.94(14)	O13-Cd3-O1	99.38(17)
O13-Cd3-O10[7]	91.01(10)	O13-Cd3-C29	101.93(17)
O13-Cd3-O3[6]	90.48(14)	Cd2[8]-O12-Cd3[9]	102.32(7)
O13-Cd3-O4[6]	112.64(16)	Cd3[10]-O10-Cd2[11]	94.99(7)
O13-Cd3-O2	95.93(14)		

[1]1-X,1-Y,1-Z; [2]+X,3/2-Y,1/2+Z; [3]1-X,-1/2+Y,1/2-Z; [4]-X,-1/2+Y,1/2-Z; [5]1-X,-1/2+Y,3/2-Z; [6]-X,-1/2+Y,3/2-Z; [7]1-X,-1/2+Y,5/2-Z; [8]1-X,1/2+Y,1/2-Z; [9]1-X,1/2+Y,3/2-Z; [10]-X,1/2+Y,1/2-Z; [11]-X,1/2+Y,3/2-Z; [12]1-X, 1/2+Y,5/2-Z

Table S2 Crystal data and structure refinement for **1**.

Identification code	**1**
Empirical formula	$C_{88}H_{68}Cd_5N_6O_{26}$
Formula weight	2187.48
Temperature/K	298.00
Crystal system	monoclinic
Space group	$P2_1/c$
a/Å	14.6903(4)
b/Å	23.3640(6)
c/Å	15.7945(5)
α /°	90
β /°	107.637(4)
γ /°	90
Volume/Å^3	5166.2(3)
Z	2
ρ_{calc}g/cm^3	1.406
μ /mm^{-1}	1.081
F(000)	2172.0
Crystal size/mm^3	0.19 × 0.16 × 0.12
Radiation	Mo K α (λ = 0.71013)
2Θ range for data collection/°	4.414 to 59.324
Index ranges	-19 ⩽ h ⩽ 19, -30 ⩽ k ⩽ 31, -20 ⩽ l ⩽ 17
Reflections collected	43446
Independent reflections	12858 [R_{int} = 0.0392, R_{sigma} = 0.0378]
Data/restraints/parameters	12858/0/567
Goodness-of-fit on F^2	1.084
Final R indexes [I>=2 σ (I)]	R_1 = 0.0353, wR_2 = 0.0906
Final R indexes [all data]	R_1 = 0.0440, wR_2 = 0.0941
Largest diff. peak/hole / e Å^{-3}	0.78/-1.12

Table S3 Structure parameters and the calculated results for gas occupancy

adsorbent	adsorbate	ρ (g/cm^3)	V_c (Å^3)	Q (mmol/g)	Gas occupancy
1	CH_4	1.41	5166.20	0.66	2.90
	C_2H_6	1.41	5166.20	2.89	12.68
	C_3H_8	1.41	5166.20	2.73	11.98

Table S4 Structure parameters and the calculated results for gas density

adsorbent	adsorbate	M(g/mol)	V_p (ml/g)	Q (mmol/g)	Gas density (g/ml)
1	CH_4	16	0.14	0.66	0.075
	C_2H_6	30	0.14	2.89	0.62
	C_3H_8	44	0.14	2.73	0.86

Table S5. Dual-site Langmuir-Freundlich parameter fits for C_3H_8 adsorption isotherms and single-site Langmuir-Freundlich parameter fit for CH_4 and C_2H_6 adsorption isotherms in **1** at 273 K.

	Site A			Site B			R^2
	$\frac{q_{A,sat}}{\text{mol/kg}}$	$\frac{b_A}{\text{kPa}^{-vA}}$	V_A	$\frac{q_{B,sat}}{\text{mol/kg}}$	$\frac{b_B}{\text{kPa}^{-vB}}$	V_B	
C_3H_8	2.05641	9.06719	1.17758	1.25372	0.10083	1.02903	0.9999
C_2H_6	3.64298	0.22672	0.88572				0.9995
CH_4	3.71753	0.00513	1.04058				0.9999

Table S6. Dual-site Langmuir-Freundlich parameter fits for C_3H_8 adsorption isotherms and single-site Langmuir-Freundlich parameter fit for CH_4 and C_2H_6 adsorption isotherms in **1** at 298 K.

	Site A			Site B			R^2
	$\frac{q_{A,sat}}{\text{mol/kg}}$	$\frac{b_A}{\text{kPa}^{-vA}}$	V_A	$\frac{q_{B,sat}}{\text{mol/kg}}$	$\frac{b_B}{\text{kPa}^{-vB}}$	V_B	
C_3H_8	1.49696	1.79808	1.27163	2.26950	0.07849	0.59306	0.9999
C_2H_6	3.33901	0.08432	0.92524				0.9996
CH_4	2.13200	0.00256	1.12150				0.9999

Table S7. Dual-site Langmuir parameter fits for C_3H_8 adsorption isotherms and single-site Langmuir parameter fit for C_2H_6 and CH_4 adsorption isotherms in **1.**

	Site A			Site B		
	$\frac{q_{A,sat}}{\text{mol/kg}}$	$\frac{b_{A0}}{\text{Pa}^{-1}}$	$\frac{E_A}{\text{kJ mol}^{-1}}$	$\frac{q_{B,sat}}{\text{mol/kg}}$	$\frac{b_{B0}}{\text{Pa}^{-1}}$	$\frac{E_B}{\text{kJ mol}^{-1}}$
C_3H_8	2.05	1.574E-12	50.4	1.25	2.561E-16	61
C_2H_6	3.4	1.107E-10	33			
CH_4	4.8	2.133E-11	27.7			

Fig. S1 Optical micrograph of **1**.

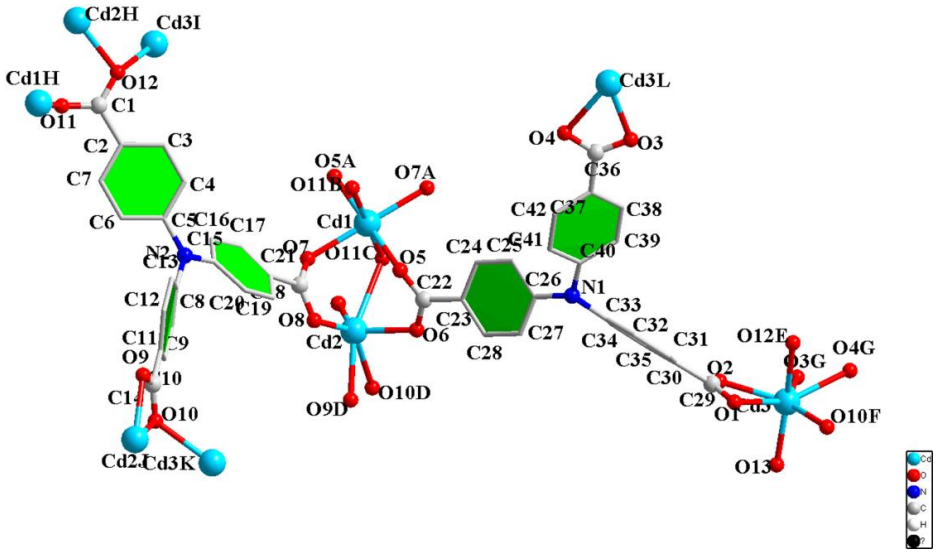

Fig. S2 The coordination environment around Cd (II) in **1**.

Symmetry codes = [A]1-x,1-y,1-z; [B]1-x,-1/2+y,1/2-z; [C]+x,3/2-y,1/2+z; [D]-x,-1/2+y,1/2-z; [E]1-x,-1/2+y,3/2-z; [F]1-x,-1/2+y,5/2-z; [G]-x,-1/2+y,3/2-z; [H]1-x,1/2+y,1/2-z; [I]1-x,1/2+y,3/2-z; [J]-x,1/2+y,3/2-z; [K]-x,1/2+y,1/2-z; [L]1-x,1/2+y,5/2-z.

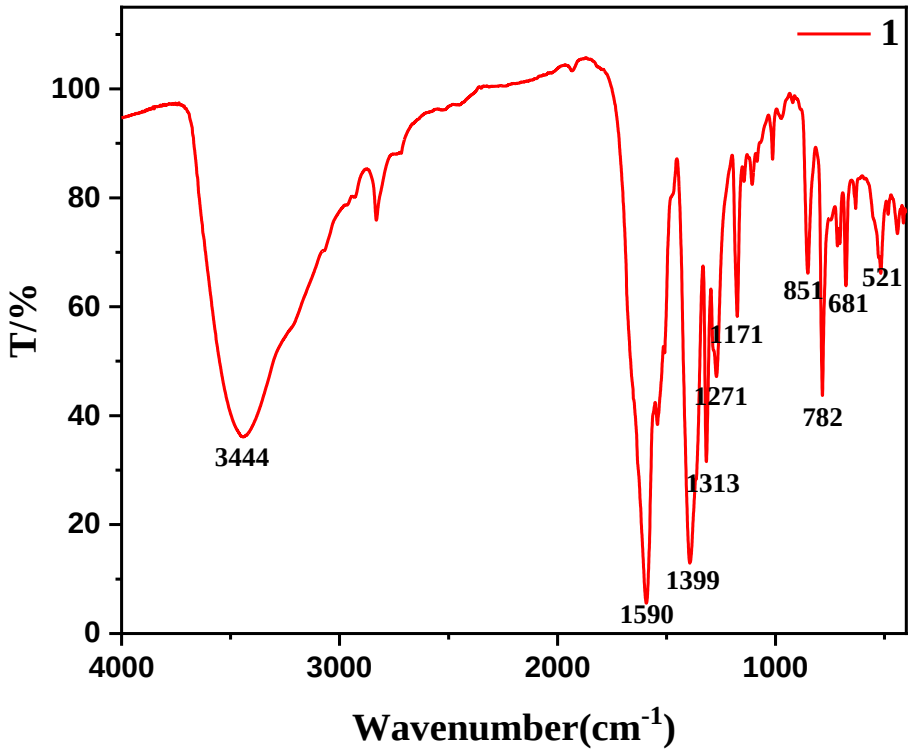

Fig. S3 IR spectra of **1**

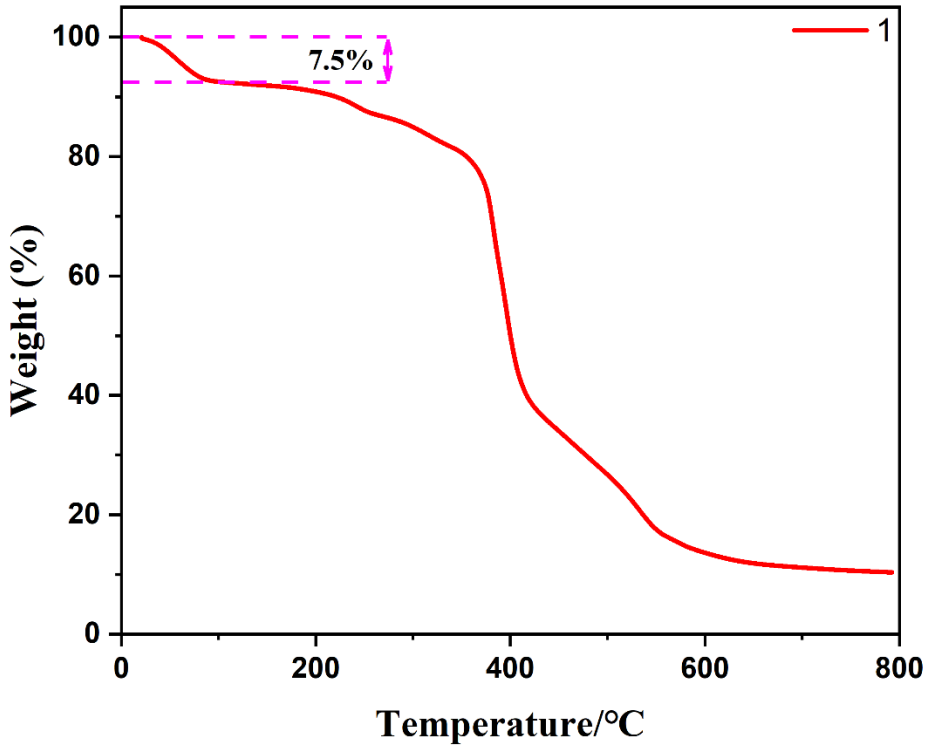

Fig. S4 The TG curves of **1**

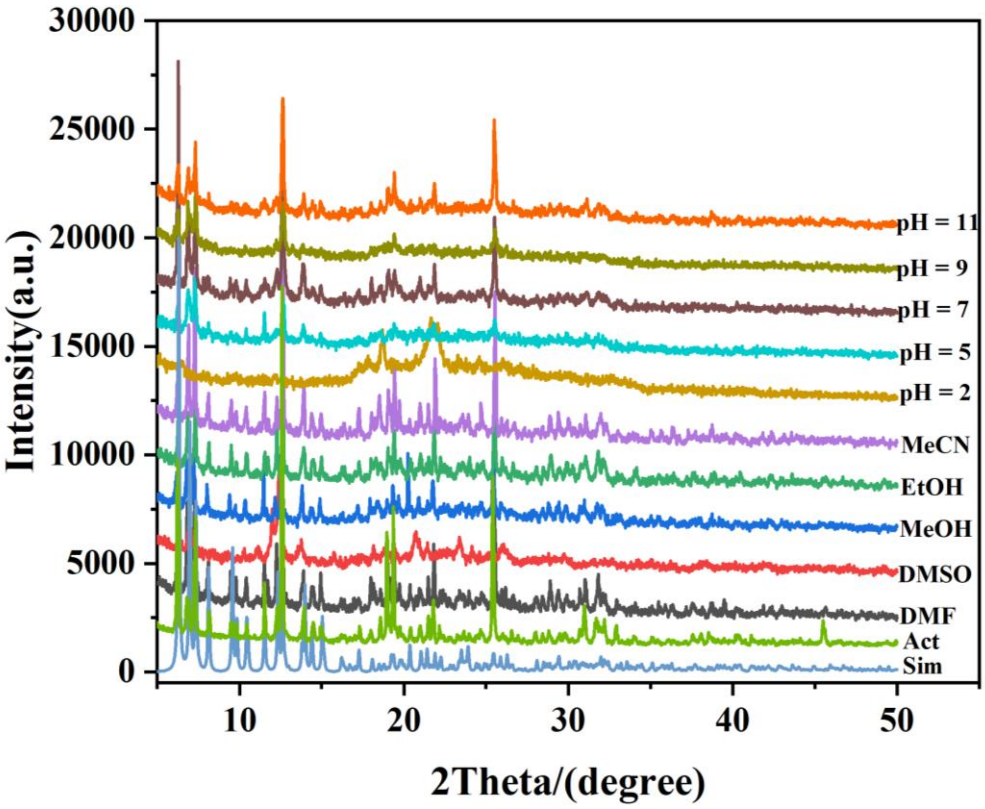

Fig. S5 The X-ray powder diffraction patterns of **1**

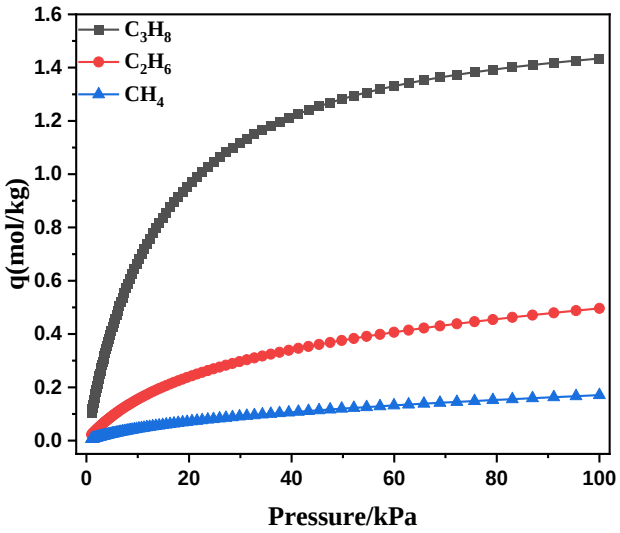

Fig. S6 The molar loadings $q_{C3H8}, q_{C2H6}, q_{CH4}$ of the three components are determined using the Ideal Adsorbed Solution Theory (IAST) of Myers and Prausnitz using the unary isotherm fits.

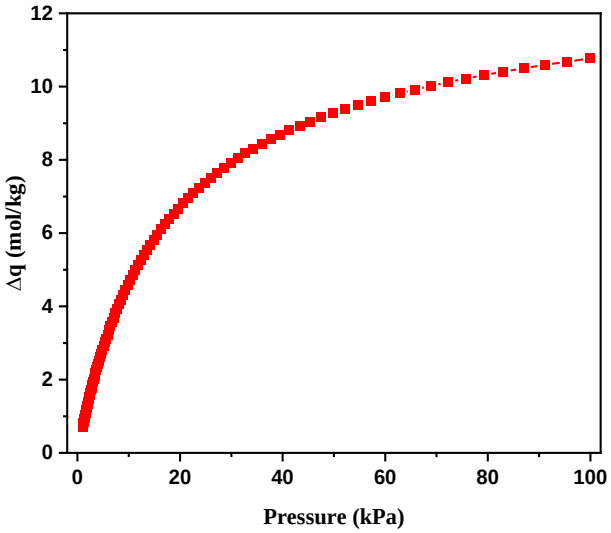

Fig. S7 IAST based separation potential for $CH_4/C_2H_6/C_3H_8$ (85/10/5) mixtures.

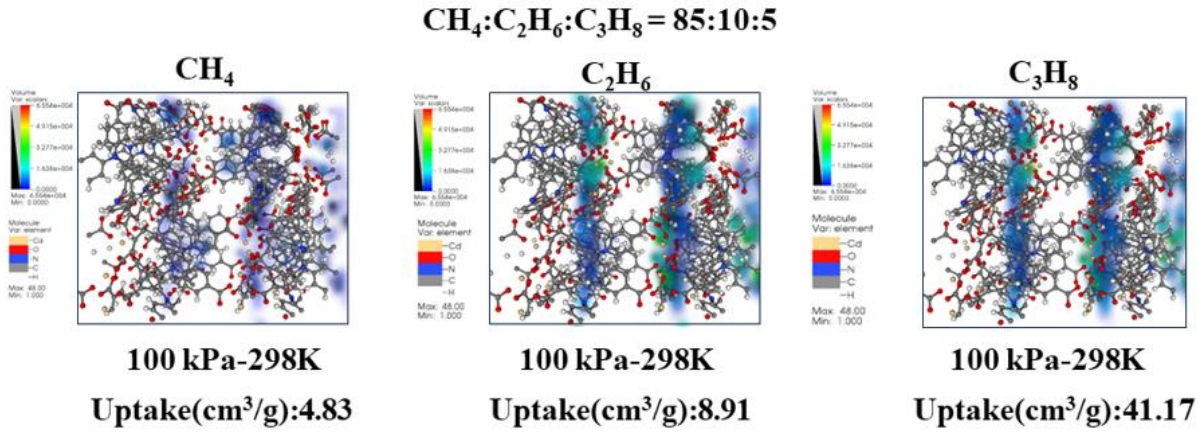

$$\Delta q = (q_{C_3H_8} + q_{C_2H_6})\frac{y_{CH_4}}{(1 - y_{CH_4})} - q_{CH_4}$$

$$\Delta q = [(41.17 + 8.91)*0.85/(1\text{-}0.85)\text{-}4.83]/22.4 = 12.67\ \text{mmol/g}$$

Fig. S8 the adsorption capacities of the ternary mixed gas in the host framework through GCMC simulations and the calculation of the separation potential (Δq).

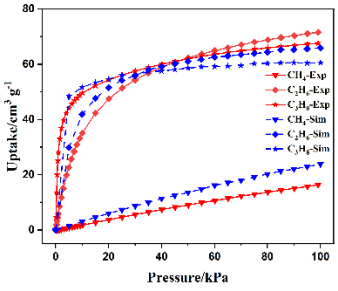

Fig.S9 GCMC simulated the single-component gas adsorption curve of $CH_4/C_2H_6/C_3H_8$ of **1** at 298 K (blue) and experimental single-component gas adsorption curve (red).

References

[1] MART & SAINT Software Reference manuals, Version 6.45 (Bruker Analytical X-ray Systems, Inc., Madison, 2003).

[2] G. M. Sheldrick, SHELXL-2014/7. Program for Refinement of Crystal Structures, University of Göttingen: Göttingen, Germany, 2014.

[3] R. Krishna, Screening Metal-Organic Frameworks for Mixture Separations in Fixed-Bed Adsorbers using a Combined Selectivity/Capacity Metric, RSC Advances 7 (2017) 35724-35737.

[4] R. Krishna, Metrics for Evaluation and Screening of Metal-Organic Frameworks for Applications in Mixture Separations, ACS Omega 5 (2020) 16987−17004.

[5] A. L. Myers; J. M. Prausnitz, Thermodynamics of Mixed Gas Adsorption, A.I.Ch.E.J. 11 (1965) 121-130.

[6] D. Dubbeldam, S. Calero, D.E. Ellis, R.Q. Snurr, RASPA: Molecular Simulation Software for Adsorption and Diffusion in Flexible Nanoporous Materials, Mol. Simulat. 42(2016) 81-101.

[7] D. Dubbeldam, K.S. Walton, T.J.H. Vlugt, S. Calero, Design, Parameterization, and Implementation of Atomic Force Fields for Adsorption in Nanoporous Materials, Adv. Theory Simulat. 2(2019) 1900135.